Stabilization of the New Antimonide $Zr_2V_6Sb_9$ by V–V and Sb–Sb Bonding

Holger Kleinke

Fb Chemie der Philipps-Universität Marburg,
Hans-Meerwein-Straße, D-35032 Marburg, Germany
Fax: (internat.) + 49(0)6421/28-8917
E-mail: kleinke@mailer.uni-marburg.de

Received April 8, 1998

Keywords: Cluster / Metal-rich antimonides / Magnetism / Sb–Sb bonds / Structure and bonding

The metal-rich antimonide $Zr_2V_6Sb_9$ has been prepared by arc-melting of stoichiometric mixtures of Zr, V, and VSb_2. $Zr_2V_6Sb_9$ is the first example of a ternary ordered (filled) variant of the unusual $V_{15}Sb_{18}$ structure type. In addition to strong metal–antimony bonding, the crystal structure is significantly stabilized by bonding V–V and Sb–Sb interactions, whereas the Zr atoms do not form short metal–metal bonds. Band structure calculations using the Extended Hückel approximation reveal $Zr_2V_6Sb_9$ being metallic, in agreement with the Pauli paramagnetism experimentally observed.

Introduction

Several different binary pnictides and chalcogenides of the valence-electron-poor ("early") transition elements with a metal/pnicogen ratio of ca. 1 or higher have been uncovered in the past[1]. Only very few antimonides and bismuthides form structures with short contacts between the pnicogen atoms Q, which are not found among the phosphides and arsenides or the chalcogenides. The fact that short Q−Q distances occur only in case of metal-rich antimonides and bismuthides can be explained with the relatively high electronegativities of phosphorus and arsenic, compared to the early transition-metal atoms. Similarly, the absence of chalcogen−chalcogen bonds in metal-rich chalcogenides can be deduced from the large differences in the electronegativities of the chalcogen atoms sulfur, selenium and tellurium on one hand and of the valence-electron-poor transition metals on the other hand. Especially the occurrence of Q−Q bonds in metal-rich antimonides appears to be somewhat special, because bismuth is classified as a metal, whereas antimony is rather a metalloid or nonmetal. From this point of view, the antimonides are the only metal-rich pnictides whose structures consist in part of nonmetal−nonmetal bonds and thus not completely reduced Q(−III) species.

The only known Bi-rich binary bismuthides of the early transition metals containing Bi−Bi bonds are $Ti_{8-x}Bi_9$ and Hf_8Bi_9[2] which crystallize in the $V_{15}Sb_{18}$ structure type[3]. As for the antimonides, ZrSb[4] and V_3Sb_2[5] both occur in structures consisting in part of hexagonal antimony layers with Sb−Sb distances between 320 pm and 325 pm. These distances are too short for van-der-Waals interactions, as a comparison with the bonding Sb−Sb contacts in the elemental form of antimony (3 × 290.8 pm and 3 × 335.5 pm) reveals[6]. It is worthwhile to note that both vanadium antimonides mentioned, i. e. $V_{15}Sb_{18}$ and V_3Sb_2, are low-temperature phases, and that no Sb−Sb contacts occur in the structure of the high-temperature form $V_{1+x}Sb$ (NiAs structure type)[7]. That leaves ZrSb and the isostructural HfSb[8] as the only binary metal-rich antimonides with Sb−Sb bonds being stable in an inert atmosphere above 1000°C with respect to disproportionation. This paper presents the synthesis, structure and properties of the new antimonide $Zr_2V_6Sb_9$. Furthermore, attempts to replace zirconium by titanium, hafnium and vanadium are discussed.

Experimental Details

The antimonides discussed below were prepared in a two-step synthesis. To avoid substantial loss of antimony during the process of arc-melting, VSb_2 was synthesized first in a fused silica tube at 650°C, starting from the elements in the stoichiometric 1:2 ratio (V: ABCR, powder, −45 micron, 99.7%, first cleaned in a 10% HCl solution, then washed with distilled water and acetone, finally dried under dynamic vacuum at approximately 500 K; Sb: MERCK, powdered, >99%). Second, stoichiometric mixtures of Zr, Ti, or Hf [Ti: VENTRON, powder, −325 mesh, 99%; Zr: ALFA, powder, 4−20 mesh, 99.6%; Hf: STREM, powder, 99.6% (including up to 2.2% Zr)], and V and VSb_2 were pressed into pellets using a force of 20 kN. The pellets were arc-melted twice after inversion under a dynamic flow of Argon (3 l/min) on a water-cooled copper hearth. The reactions of the starting compositions "$M_2V_6Sb_9$" (with M = Ti, Zr, Hf) led to homogenous products, according to the powder diagrams obtained with Cu-$K_{\alpha 1}$ radiation (λ = 154.05 pm, using silicon as internal standard). The lattice dimensions as obtained from the powder diagrams are listed in Table 1. In addition to the fact that here the $V_{15}Sb_{18}$ structure type was found after the rapid cooling in the arc melter, the significant increase of the lattice dimensions in comparison to $V_{15}Sb_{18}$ prove the incorporation of the larger atoms of the titanium group.

Attempts to determine the phase range of $Zr_{2-x}V_{6+x}Sb_9$ did not result in homogenous samples when $x \neq 0$. The

 © WILEY-VCH Verlag GmbH, D-69451 Weinheim, 1998 1434−1948/98/0909−1369 $ 17.50+.50/0

Table 1. Comparison of lattice dimensions

Starting composition	Empirical formula[a]	Side products[b]	*a*/pm	*c*/pm	$V/10^6$pm^3
1V, 1Sb (ref.[3])[a]	$V_{7.46(3)}Sb_9$	?	958.66(5)	704.74(5)	647.68
1.2V, 1Sb[a]	$V_{7.49(1)}Sb_9$	V_3Sb_2	959.2(1)	705.46(7)	649.1
2Ti, 6V, 9Sb[b]			966.3(3)	709.9(3)	662.9
0.3 Zr, 7.7V, 9Sb[b]		$V_{1+x}Sb$	969.0(2)	713.2(3)	669.7
1Zr, 7V, 9Sb[b]		$V_{1+x}Sb$	973.6(4)	715.9(4)	678.6
1Zr, 7V, 9Sb[a]	$Zr_{1.61(6)}V_{6.41}Sb_9$[c]		973.2(1)	716.66(8)	678.8
2Zr, 6V, 9Sb[b]			973.4(6)	716.8(4)	679.2
2Zr, 6V, 9Sb[a]	$Zr_{1.80(4)}V_{6.20}Sb_9$[c]		973.7(2)	716.5(2)	679.3
3Zr, 5V, 9Sb[b]		ZrSb	977.7(1)	717.9(1)	686.2
3Zr, 5V, 9Sb[a]	$Zr_2V_6Sb_9$		978.3(1)	719.5(1)	688.6
2Hf, 6V, 9Sb[b]			975.7(2)	721.7(3)	687.1

[a] Single crystal data. – [b] Powder data. – [c] Obtained with the postulation of mixed Zr/V but full occupation of the "Zr1" and "Zr2" sites.

Zr-poor samples contained $V_{1+x}Sb$, and the Zr-rich phases ZrSb. EDX investigations of selected crystals showed only a minor phase range of $Zr_{2-x}V_{6+x}Sb_9$, i. e. the Zr content varied from 7 to 15 atom-%. These variations may in part be due to different orientations of the crystals to the incident beam. Indexing of the powder diagrams, however, led to different lattice dimensions of the $Zr_{2-x}V_{6+x}Sb_9$ phases, which increase with increasing x (see Table 1). This is a consequence of the larger atomic radius of zirconium, compared to vanadium. However, based on the fact that the V(1) site is not completely occupied in the structure of $V_{15}Sb_{18}$, it may be possible that comparable voids occur in the structures of the $Zr_{2-x}V_{6+x}Sb_9$ phases.

In order to determine the site preferences of the Zr atoms, plate-like single crystals were selected for structure investigations of the phases of the starting compositions "$Zr_1V_7Sb_9$", "$Zr_2V_6Sb_9$" and "$Zr_3V_5Sb_9$". In all three cases, the unit-cell dimensions obtained from the single-crystal diffractometer were in good agreement with those calculated from the powder diagrams of the corresponding bulk samples. In all cases, numerical absorption corrections were performed.

As a starting model, the atomic positions of the binary antimonide $V_{15}Sb_{18}$ were used. The V(1) and V(2) positions were tentatively assigned to Zr sites, because of the higher Sb coordination numbers [eight for V(1) and V(2), and six for V(3) and V(4)]. The refinements of the three different data sets (using SHELXL93[9]) converged smoothly to reasonable residual factors, i. e. conventional R values of $R(F)$ = 0.0316 for "$Zr_1V_7Sb_9$", $R(F)$ = 0.0216 for "$Zr_2V_6Sb_9$" and $R(F)$ = 0.0342 for "$Zr_3V_5Sb_9$". Since the thermal displacement parameters of the Zr positions of the first two data sets were significantly higher than those of the V sites, and at least some mixed occupancies were expected because of the differences in the lattice dimensions, the occupancy factors of all metal sites were refined in order to check for deviations from the ideal stoichiometries. Only the occupancy factors of the Zr sites of the first two data sets differed more than 2% from 100%. Since these sites are completely filled in case of "$Zr_3V_5Sb_9$", corresponding to the formula $Zr_2V_6Sb_9$, they were refined as being statistically mixed occupied by Zr and V to 100% in cases of "$Zr_1V_7Sb_9$" and "$Zr_2V_6Sb_9$". This model led in both cases to more uniform displacement parameters and lower residual factors [R(F) = 0.0295 for "$Zr_1V_7Sb_9$" and $R(F)$ = 0.0210 for "$Zr_2V_6Sb_9$"]. The formulas were finally refined to $Zr_{1.61(6)}V_{6.39}Sb_9$, $Zr_{1.80(4)}V_{6.20}Sb_9$, and $Zr_2V_6Sb_9$, respectively. More details about the structure determinations are given in Table 2[10], and atomic parameters are listed in Table 3. It should be noted, however, that two other models, based on the occurrence of voids, would also be in agreement with these experimental data. First, the assumption of no incorporation of V on the Zr sites would result in the formulas $Zr_{1.85(2)}V_6Sb_9$ and $Zr_{1.93(2)}V_6Sb_9$, and second, one might also assume voids, V and Zr atoms on the two Zr sites.

Results and Discussion

$Zr_2V_6Sb_9$ is the first ternary ordered substitution variant of the $V_{15}Sb_{18}$ structure type. For easier comparisons, the setting and the atomic labeling of $V_{15}Sb_{18}$ are used throughout this article, but, of course, V(1) and V(2) of $V_{15}Sb_{18}$ are replaced by Zr(1) and Zr(2). The structure of $Zr_2V_6Sb_9$ is shown in a projection along the crystallographic c axis in Figure 1.

The $Zr_2V_6Sb_9$ structure contains chains of face-sharing square Zr-centered Sb_8 antiprisms, which are surrounded by V layers, where the V atoms are situated in severely distorted Sb_6 octahedra. The Zr(1) and Zr(2) atoms, alternating in each chain along [001], have different distances to the eight surrounding Sb atoms, i. e. 4 × 305.1(2) pm and 4 × 309.2(2) pm for Zr(1), and 4 × 293.2(2) pm and 4 × 293.4(1) pm for Zr(2). The latter distances correspond to those found in the ternary ZrNiSb [TiNiSi-type, five Zr–Sb bonds per Zr atom between 291.44(7) pm and 296.65(6) pm][11]. The differences in the averaged bond lengths occur

Table 2. Crystallographic data for $Zr_{2-x}V_{6+x}Sb_9$

Empirical formula	$Zr_{1.61(6)}V_{6.39}Sb_9$[a]	$Zr_{1.80(4)}V_{6.20}Sb_9$[a]	$Zr_2V_6Sb_9$
Molar mass	1568.12 g/mol	1575.77 g/mol	1583.83
Temp. of data collection	295 K		
Crystal size/mm	0.14 × 0.04 × 0.003	0.08 × 0.02 × 0.007	0.12 × 0.10 × 0.07
Space group	*P*4/*nmm* (No. 129)		
a/pm	973.2(1)	973.7(2)	978.3(1)
c/pm	716.66(8)	716.5(2)	719.5(1)
V/(10^6 pm^3)	678.8(1)	679.3(2)	688.6(1)
Radiation	Mo-$K\alpha_1$, λ = 71.609 pm		
No. of formula units; *F*(000)	2; 1341	2; 1347	2; 1354
Calculated density	7.67 g/cm^3	7.70 g/cm^3	7.64 g/cm^3
Absorption coefficient	228.7 cm^{-1}	228.7 cm^{-1}	225.8 cm^{-1}
Range of 2θ		3°−60°	
No. of independent reflections	609 (R_{int} = 0.081)	593 (R_{int} = 0.045)	616 (R_{int} = 0.103)
No. of observed reflections [$I > 2\sigma(I)$]	457	453	434
No. of parameters	34	34	32
$R(F)$, $R_w(F^2)$, GOF	0.030, 0.059, 1.05	0.021, 0.036, 1.07	0.034, 0.064, 1.02
Extinction coefficient	0.0007(2)	0.0007(1)	0.0011(2)
Max., min. peak in final diff. map	3.05 e$^-$/(10^6 pm^3), −1.99 e$^-$/(10^6 pm^3)	1.43 e$^-$/(10^6 pm^3), −1.41 e$^-$/(10^6 pm^3)	2.20 e$^-$/(10^6 pm^3), −1.81 e$^-$/(10^6 pm^3)

[a] See Table 1.

Table 3. Positional parameters and equivalent displacement factors for $Zr_2V_6Sb_9$

Atom	site	*x*	*y*	*z*	U_{eq}/(10^4 pm^2)
Zr(1)	2c	1/4	1/4	0.9164(3)	0.0102(5)
Zr(2)	2c	1/4	1/4	0.4132(3)	0.0069(4)
V(3)	4d	0	0	0	0.0077(5)
V(4)	8i	3/4	0.3910(2)	0.1621(3)	0.0070(4)
Sb(1)	2c	3/4	1/4	1/2	0.0127(4)
Sb(2)	8j	0.92206(5)	0.92206(5)	0.3488(1)	0.0102(2)
Sb(3)	8i	3/4	0.99776(8)	0.81671(9)	0.0082(2)

Figure 1. Projection of the structure of $Zr_2V_6Sb_9$ along [001]; large, white circles: Zr; small, black: V; medium, gray: Sb; metal−Sb bonds omitted for clarity

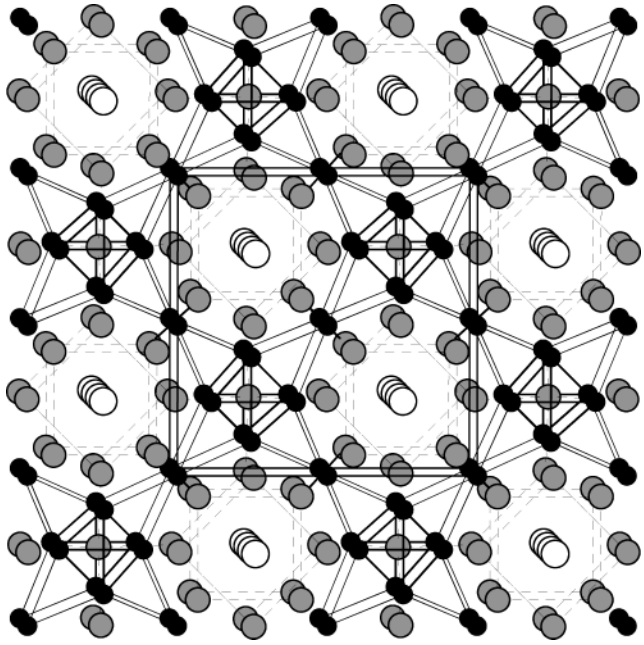

to a comparable extent in the structures of $V_{15}Sb_{18}$ and $Ti_{8-x}Bi_9$ (17.2 pm in both structures), also. The V(1) position, being the one which is occupied only to 50% in the structure of $V_{15}Sb_{18}$, shows very high displacement parameters. Similarly, the displacement parameters of that position in $Zr_2V_6Sb_9$ and $Ti_{8-x}Bi_9$ are approximately between 50% and 100% higher than those of the other metal sites, but the position is filled completely in both cases. The high displacement parameters can be understood as a consequence of the large metal−pnicogen distances, pointing to a "rattling" in a large Sb_8 (or Bi_8) cage, which might result in an unusually low thermal conductivity, as observed for the antimonides LnM_4Sb_{12} (M = Fe, Co, …)[12].

Each V atom in $Zr_2V_6Sb_9$ is situated in a distorted Sb_6 octahedron with V−Sb distances between 271.3(2) pm and 283.1(1) pm. The averaged distances are slightly enlarged compared to the distances in $V_{15}Sb_{18}$ [between 272.3(4) pm and 279.2(2) pm]. The shorter V−Sb distances, compared to the Zr−Sb distances, most likely inhibit a significant incorporation of the larger Zr atoms on the V positions. The V layers (Figure 2) contain V(4) tetrahedra, which are interconnected via common V(3) atoms capping four edges of each V(4) tetrahedron.

The description based on V tetrahedra should not imply the existence of localized bonds within the tetrahedral units. In contrast, the V−V bonds between the tetrahedra and the bridging V(3) atoms are shorter than the edges capped by the V(3) atoms [291.2(1) pm vs. 304.2(3) pm]. The shortest V−V bond [275.9(4) pm] is situated at the edge of the tetrahedron capped by an Sb(1) atom. The lengths of these bonds are just between the two shortest distances observed in the body-centered cubic (*bcc*) element V (262 pm and 303 pm)[13].

The Sb_4 units of the $ZrSb_8$ square antiprisms are exactly planar squares with Sb−Sb distances of 336.65(9) pm in the $Sb(2)_4$ square and 342.76(8) pm in the $Sb(3)_4$ plane. These

Figure 2. Projection of the V layer along the slightly tilted *c* axis

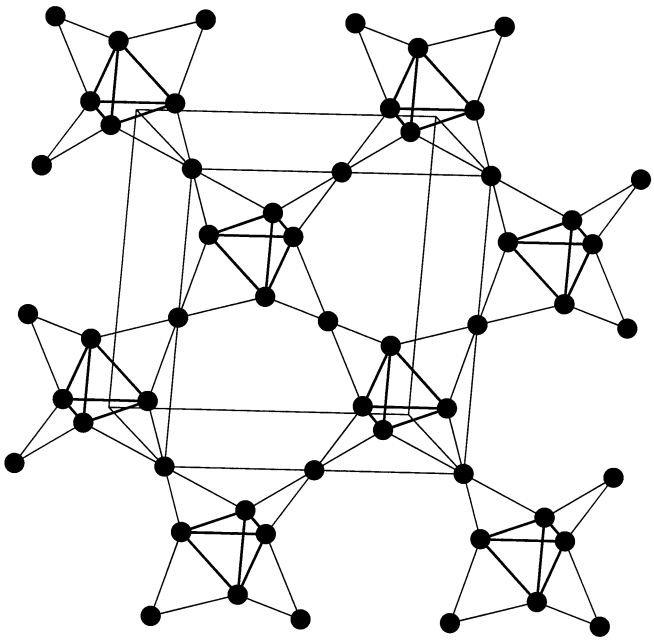

Figure 3. Projection of the puckered Sb(1),Sb(3) layer along the slightly tilted *c* axis

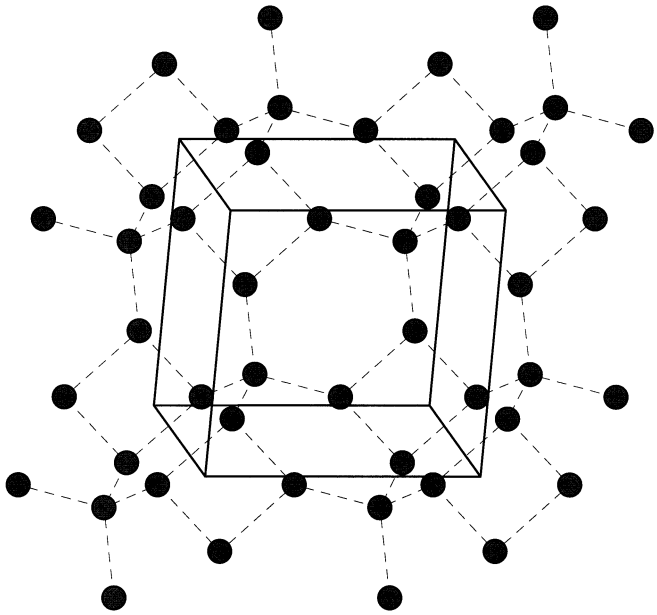

Figure 4. Projection of the puckered Sb(2) layer along the slightly tilted *c* axis

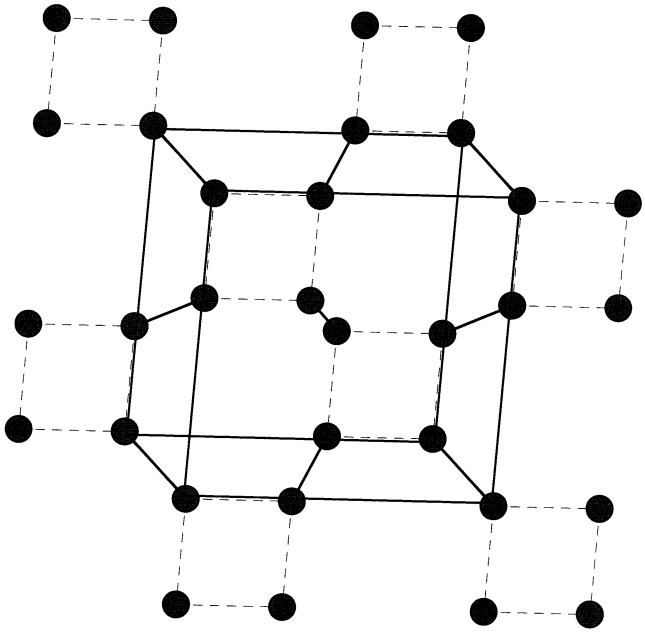

distances, being significantly larger than in the structure of $V_{15}Sb_{18}$ [319.0(1) pm and 322.9(1) pm], may be compared to the second shortest Sb−Sb bonds in elemental antimony of 335.5 pm. The latter, connecting the layers in the element, have to have bonding character because elemental antimony does not exhibit two-dimensional physical properties. The similar lengths in case of the structure of $Zr_2V_6Sb_9$ might occur with similar bond strengths, however, the shorter contacts of ca. 320 pm in $V_{15}Sb_{18}$ correspond most likely to stronger, but still somewhat weak, Sb−Sb bonds. Three causes complement each other: first, the larger size of Zr, compared to V, results in enlarged lattice parameters and therefore in longer Sb−Sb separations; second, the higher amount of valence electrons of the Zr phase (4.22 vs. 4.17 per Sb atom) and third the lower electronegativity of Zr, compared to V, both lead to higher negatively charged Sb atoms in case of $Zr_2V_6Sb_9$. As a consequence, more antibonding Sb−Sb states are filled in case of $Zr_2V_6Sb_9$, compared to $V_{15}Sb_{18}$, leading to weaker net bonding.

Additional Sb−Sb interactions between the Sb(1) and Sb(3) atoms of comparable length [335.89(7) pm] connect the $Sb(3)_4$ planes to infinite puckered layers consisting of planar Sb_4 and Sb_6 rings, as emphasized with dashed lines in Figure 3. The latter rings were also observed in the structure of the low-temperature phase V_3Sb_2 with shorter Sb−Sb distances of 320 pm.

On the other hand, the Sb(2) squares are interconnected via the shortest Sb−Sb contacts in this structure [306.3(2) pm] to puckered layers, which contain puckered eight-membered Sb(2) rings in addition to the $Sb(2)_4$ squares. The short Sb−Sb bonds are shown as bold lines in Figure 4, whereas the longer distances of 336.65(9) pm correspond to the dashed lines.

The Sb(2)−Sb(2) distance of 306.3(2) pm may be compared to other intermediate Sb−Sb distances in rather Sb-rich phases without metal−metal bonding, such as $LaCrSb_3$ with distances between 305.81(5) pm and 317.5(2) pm[14] and La_3TiSb_5 with a linear Sb chain consisting of Sb−Sb separations of 314.00(5) pm[15]. In both cases, it was concluded that all electrons from the metal atoms were transferred to the Sb atoms, leading to the tentative ionic formulations $(La^{3+})(Cr^{3+})(Sb^{2.5-})_2(Sb^{1-})$ and $(La^{3+})_3(Ti^{4+})(Sb^{3-})_3(Sb^{2-})_2$. These assignments are in agreement with a consideration of the above mentioned

Sb−Sb contacts as 1-electron-2-center bonds in a local view. In case of $Zr_2V_6Sb_9$, a comparable classification is less straightforward because of the different V−V bond lengths and the occurrence of the longer Sb−Sb distances > 330 pm. Neglecting the longer Sb−Sb distances and considering the shortest Sb−Sb bond as a one-electron bond would result in the formal ionic formulation $(Zr^{4+})_2(V^{2.83+})_6(Sb^{3-})_5(Sb^{2.5-})_4$, if one also ignores in a zeroth approximation the large Zr−Zr and Zr−V distances (> 350 pm). The ionic formulation is not meant to imply ionic character of $Zr_2V_6Sb_9$, but it may be helpful in understanding the bonding situation. According to this electron counting, 2.17/6 = 0.36 electrons remain available for V−V bonding per V atom, i. e. four V−V bonds per V(3) atom [291.2(1) pm] and five V−V bonds per V(4) atom [between 275.9(4) pm and 304.2(3) pm]. This very crude approximation gives an explanation for the occurrence of fractional bond orders of the V−V and Sb−Sb bonds. In case of $V_{15}Sb_{18}$, a similar discussion would result in the electron counting scheme $(V^{5+})_3(V^{2.92+})_{12}(Sb^{3-})_{10}(Sb^{2.5-})_8$, and therefore 0.35 electrons for each V(3) and V(4) atom to form V−V bonds. In the latter case, however, the Sb−Sb contacts of ca. 320 pm should not be neglected.

Calculations of the electronic structure using the Extended Hückel approximation (EH)[16,17,18] were performed in order to evaluate the bonding situation (and the physical properties) of the structure of $Zr_2V_6Sb_9$. Since the standard values of the metal parameters are usually energetically lower than the parameters in low-valent compounds, the metal parameters were optimized by charge iteration of vanadium in $V_{15}Sb_{18}$ with constant Sb parameters[19], followed by the optimization of zirconium in $Zr_2V_6Sb_9$. The parameters used are summarized in Table 4. The calculated densities of states (Figure 5) show a significant number of states at the Fermi level, which basically are centered at the vanadium atoms. The Zr orbitals are much less filled than the V orbitals, confirming the electron-counting scheme mentioned above. The *p* states of antimony are found in a wide peak between −10 eV and −15.5 eV, with a tail going up above the Fermi level. The latter is a hint to not completely reduced antimony ions, in agreement with the occurrence of rather small Sb−Sb distances. The fact that the Sb(2) atoms have shorter Sb−Sb contacts, compared to Sb(1) and Sb(3), expresses itself in smaller Mulliken gross populations calculated with the EH method [Sb(2): 5.23; Sb(3): 5.35; Sb(1): 5.53 electrons], supporting the trend implied but certainly overestimated by the electron-counting scheme $(Zr^{4+})_2(V^{2.83+})_6(Sb^{3-})_5(Sb^{2.5-})_4$. The differences between Sb(1) and Sb(3) also show the treatment of both atoms as Sb^{III} as being a crude approximation. Furthermore, the covalent mixing of the Sb states with the V and Zr states, as can be seen from the contribution of the *d* states of both different kinds of metal atoms to the Sb peak below −11 eV, imply $Zr_2V_6Sb_9$ being a compound with covalent Zr−Sb and V−Sb interactions.

The vanadium substructure with fractional V−V bonds should occur with metallic properties in the *a*,*b* plane, especially under consideration of the huge contribution of V states to the densities of states at the Fermi level. In addition, the occurrence of Zr states at the Fermi level and the somewhat long Zr−Zr distances parallel to the *c* axis might lead to metallic conductivity along the *c* direction, also. However, since the antimony atoms, having holes in the *sp* band, certainly contribute to the metallic properties, three-dimensional metallic properties are assumed. The temperature-independent Pauli paramagnetism experimentally obtained from the $Zr_2V_6Sb_9$ bulk sample (Figure 6) shows the presence of itinerant electrons, and thus metallic properties, but it provides no information on the dimensionality of the physical properties. Attempts to synthesize crystals suitable for direction dependent measurements were unsuccessful.

Table 4. Parameters used for EH calculations on $Zr_2V_6Sb_9$

Orbital	H_{ii}/eV	ζ_1	c_1	ζ_2	c_2
Zr, 5s	−8.204	1.82			
Zr, 5p	−4.593	1.78			
Zr, 4d	−8.117	3.84	0.6213	1.51	0.5798
V, 4s	−7.894	1.30			
V, 4p	−4.304	1.30			
V, 3d	−8.510	4.75	0.4755	1.70	0.5798
Sb, 5s	−18.80	2.32			
Sb, 5p	−11.70	2.00			

Figure 5. Calculated densities of states for $Zr_2V_6Sb_9$; horizontal line: Fermi level; solid line: total DOS; long dashes: Zr contribution; short dashes: V; dots: Sb

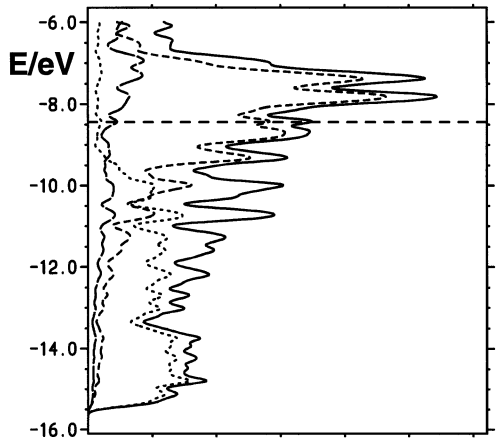

A discussion of the total crystal orbital overlap populations of all Zr−Sb, V−Sb and V−V interactions is instructive. These interactions are depicted in Figure 7, whereas the Zr−Zr states are neglected because of their small contributions. Mainly bonding interactions are found between −15.5 eV and the Fermi level at −8.44 eV, which are dominated by the V−Sb bonds. Only very few antibonding V−Sb states are filled below the Fermi level. Although the Zr−Sb peak area is roughly half as large as the V−Sb peak area, the Zr−Sb interactions play a similar role per bond, because 2 × 8 = 16 Zr−Sb bonds and 6 × 6 = 36 V−Sb bonds exist per formula unit. The V−V bonds are precisely optimized in the structure of $Zr_2V_6Sb_9$, according to the results of the EH calculations. Altogether,

Figure 6. Temperature dependence of the magnetic susceptibility of $Zr_2V_6Sb_9$

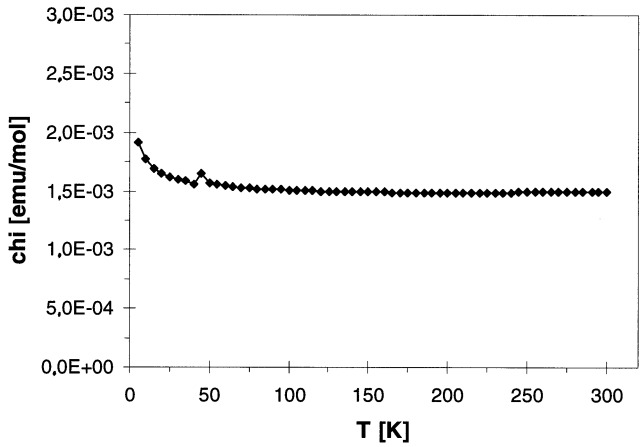

the V−V interactions play a minor but still significant role for the stability of $Zr_2V_6Sb_9$, compared to the Zr−Sb and V−Sb bonds. This can be taken from a rough optical estimation of the sizes of the different areas under the different COOP curves as shown in Figure 7, which reflect the different sums of the overlap populations. This simplistic view should be regarded cautiously, because a Zr−Sb bond may be a much stronger bond than a V−V bond of a comparable overlap population.

Figure 7. Selected total COOP curves for $Zr_2V_6Sb_9$; horizontal line: Fermi level; solid line: V−V interactions; long dashes: Zr−Sb; short dashes: V−Sb; right part of the diagram: bonding interactions (+); left: antibonding (−)

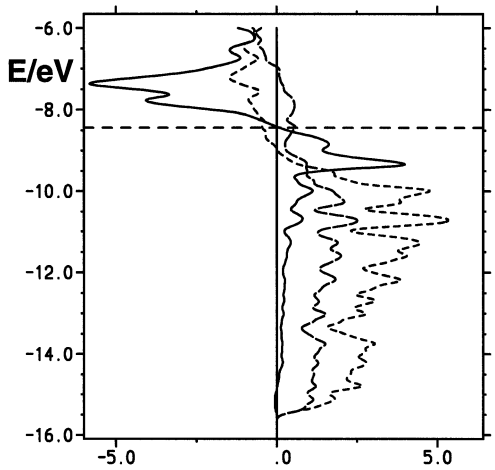

The concrete Mulliken overlap populations (MOPs) of selected interatomic interactions are listed in Table 5. The V−V interactions have significant positive MOP values, ranging from 0.184 and 0.096 within the tetrahedral units to 0.145 for every V(3)−V(4) bond. This may be compared to the values calculated for the shortest interaction of 262 pm (0.298) and for the longer ones of 303 pm (0.120) in elemental vanadium[20]. As proposed above, the Zr−Zr and Zr−V interactions have only weak bonding character, if any, with overlap populations between 0.029 and 0.065 electrons per bond. Similar values (i.e. between 0.025 and 0.048) also are found for the Sb−Sb interactions between 330 pm and 350 pm. The small positive net overlap populations are the result of the sum of bonding and antibonding Sb−Sb states, as shown in the averaged Sb−Sb COOP curves in Figure 8. The positive but small values point to weak bonding character for these interactions. The overlap population of 0.077 for the comparable Sb−Sb bond in elemental antimony (335.5 pm) is of the same magnitude.

Table 5. Selected interatomic distances and overlap populations of $Zr_2V_6Sb_9$

interaction	length/pm	MOP[a]
Zr(1)−1 Zr(2)	357.4(3)	0.041
Zr(1)−1 Zr(2)	362.1(3)	0.065
Zr(1)−4 V(3)	351.06(5)	0.053
Zr(1)−4 V(4)	355.7(2)	0.029
Zr(1)−4 Sb(2)	305.1(2)	0.234
Zr(1)−4 Sb(3)	309.2(2)	0.239
Zr(2)−4 Sb(2)	293.2(2)	0.422
Zr(2)−4 Sb(3)	293.4(1)	0.453
V(3)−4 V(4)	291.2(1)	0.145
V(3)−2 Sb(2)	273.2(1)	0.388
V(3)−4 Sb(3)	277.87(4)	0.302
V(4)−1 V(4)	275.9(4)	0.184
V(4)−2 V(4)	304.2(3)	0.096
V(4)−1 Sb(1)	279.5(2)	0.411
V(4)−2 Sb(2)	282.5(2)	0.348
V(4)−1 Sb(3)	271.3(2)	0.382
V(4)−2 Sb(3)	283.1(1)	0.245
Sb(1)−4 Sb(3)	335.89(7)	0.048
Sb(2)−1 Sb(2)	306.3(2)	0.339
Sb(2)−2 Sb(2)	336.65(9)	0.042
Sb(3)−2 Sb(3)	342.76(8)	0.025

[a] MOP = Mulliken Overlap Population [electrons per bond].

Figure 8. Selected averaged COOP curves for $Zr_2V_6Sb_9$; horizontal line: Fermi level; solid line: Sb−Sb interactions < 310 pm; dashed: Sb−Sb interactions between 310 pm and 350 pm; right part of the diagram: bonding interactions (+); left: antibonding (−)

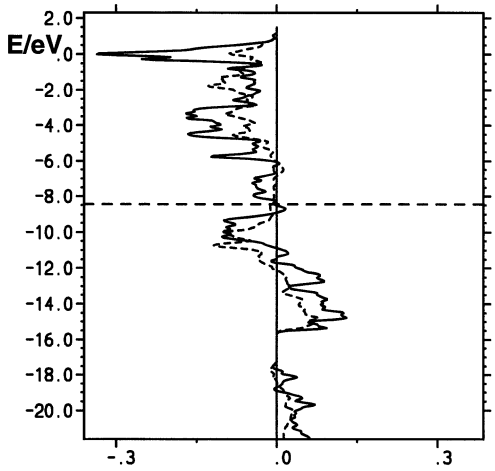

Fewer antibonding states are filled in case of the shortest Sb−Sb interaction in the structure of $Zr_2V_6Sb_9$ [d = 306.3(2) pm, MOP = 0.339]. The COOP curves also show the presence of antibonding Sb−Sb states above the Fermi level, supporting the model of not completely reduced Sb^{III}

anions. For an evaluation of the bond strength, the short Sb−Sb bond may be compared with shorter Sb−Sb bonds, i.e. in the element (d = 290.8 pm, MOP = 0.530[20]), with the Sb_2 pair in (α-)$ZrSb_2$ (d = 288 pm, MOP = 0.51[4]) or the $^1_\infty[Sb^{1-}]$ chain in KSb with $\bar{d}$ = 284 pm[21] and an averaged MOP of 0.645[20]. Since the latter bonds may be described to a first estimation as 2-electrons-2-center bonds (i. e. corresponding to a bond order of one), the crude approximation of a half bond order for the short Sb−Sb bond in $Zr_2V_6Sb_9$ is supported by the calculations of the electronic structure. It is thus concluded that the Sb−Sb interactions contribute significantly to the formation energy of $Zr_2V_6Sb_9$, although $Zr_2V_6Sb_9$ is to be considered a low-valent antimonide because of the V−V bonds.

[1] P. Villars, *Pearson's Handbook*, Materials Park, Ohio 44073, **1997**.
[2] C. G. Richter, W. Jeitschko, *J. Solid State Chem.* **1997**, *134*, 26−30.
[3] S. Furuseth, H. Fjellvåg, *Acta Chem. Scand.* **1995**, *49*, 417−422.
[4] E. Garcia, J. D. Corbett, *J. Solid State Chem.* **1988**, *73*, 452−467.
[5] J. Steinmetz, B. Malaman, B. Roques, *C. R. Acad. Sci., Ser C* **1977**, *284 C,* 499−502.
[6] C. S. Barrett, P. Cucka, K. Haefner, *Acta Crystallogr.* **1963**, *16*, 451−453.
[7] J. Bouwma, C. F. van Bruggen, C. Haas, *J. Solid State Chem.* **1973**, *7*, 255−261.
[8] W. Rossteutscher, K. Schubert, *Z. Metallk.* **1965**, *56*, 813−822.
[9] G. M. Sheldrick, *SHELX93*, University of Göttingen, **1993**.
[10] Further details of the crystal-structure investigations may be obtained from the Fachinformationszentrum Karlsruhe, D-76344 Eggenstein-Leopoldshafen, Germany, on quoting the depository numbers CSD-408567, -408566, and -408565.
[11] H. Kleinke, *Z. Anorg. Allg. Chem.*, in press.
[12] B. C. Sales, D. Mandrus, R. K. Williams, *Science* **1996**, *272*, 1325−1328.
[13] Y. N. Smirnov, V. A. Finkel, *Sov. Phys. − JETP (Engl. Transl.)* **1966**, *22*, 750−753; *Chem. Abstr.* **1966**, *64*, 4365.
[14] M. J. Ferguson, R. W. Hushagen, A. Mar, *J. Alloys Compd.* **1997**, *249*, 191−198.
[15] G. Bolloré, M. J. Ferguson, R. W. Hushagen, A. Mar, *Chem. Mater.* **1995**, *7*, 2229−2231.
[16] R. Hoffmann, *J. Chem. Phys.* **1963**, *39*, 1397−1412.
[17] M.-H. Whangbo, R. Hoffmann, *J. Am. Chem. Soc.* **1978**, *100*, 6093−6098.
[18] Program EHMACC, adapted for use on a PC by M. Köckerling, Gesamthochschule Duisburg, **1997**.
[19] E. Clementi, C. Roetti *At. Nucl. Data Tables* **1974**, *14*, 177.
[20] H. Kleinke, unpublished calculations.
[21] W. Hönle, H.-G. von Schnering, *Z. Kristallogr.* **1981**, *155*, 307−314.

[98082]